Covalency competition dominates the water oxidation structure-activity relationship on spinel oxides

Sun, Yuanmiao; Liao, Hanbin; Wang, Jiarui; Chen, Bo; Sun, Shengnan; Ong, Samuel Jun Hoong; Xi, Shibo; Diao, Caozheng; Du, Yonghua; Wang, Jia-Ou; Breese, Mark B. H.; Li, Shuzhou; Zhang, Hua; Xu, Jason Zhichuan

2020

Sun, Y., Liao, H., Wang, J., Chen, B., Sun, S., Ong, S. J. H., Xi, S., Diao, C., Du, Y., Wang, J., Breese, M. B. H., Li, S., Zhang, H. & Xu, J. Z. (2020). Covalency competition dominates the water oxidation structure-activity relationship on spinel oxides. Nature Catalysis, 3, 554-563. https://dx.doi.org/10.1038/s41929-020-0465-6

https://hdl.handle.net/10356/148451

https://doi.org/10.1038/s41929-020-0465-6

Covalency Competition Dominates the Water Oxidation Structure-Activity Relationship on Spinel Oxide

Yuanmiao Sun[1,Δ], Hanbin Liao[1,2Δ], Jiarui Wang[1,3], Bo Chen[1], Shengnan Sun[1,11], Samuel Jun Hoong Ong[1,3], Shibo Xi[4], Caozheng Diao[5], Yonghua Du[4,12], Jiaou Wang[6], Mark B.H. Breese[5], Shuzhou Li[1], Hua Zhang[7,8], Zhichuan J. Xu[1, 9,10]*

[1]School of Materials Science and Engineering, Nanyang Technological University, 50 Nanyang Avenue, Singapore 639798, Singapore.

[2]The Cambridge Centre for Advanced Research and Education in Singapore, 1 CREATE Way, Singapore 138602, Singapore.

[3]Singapore-HUJ Alliance for Research and Enterprise (SHARE), Nanomaterials for Energy and Energy-Water Nexus (NEW), Campus for Research Excellence and Technological Enterprise (CREATE), Singapore 138602, Singapore.

[4]Institute of Chemical and Engineering Science A*Star, 1 Pesek Road, Singapore 627833, Singapore.

[5]Singapore Synchrotron Light Source (SSLS), 5 Research Link, National University of Singapore, Singapore 117603, Singapore.

[6]Beijing Synchrotron Radiation Facility, Institute of High Energy Physics, Chinese Academy of Sciences, Beijing 100049, China.

[7]Department of Chemistry, City University of Hong Kong, Hong Kong, China.

[8]Hong Kong Branch of National Precious Metals Material Engineering Research Center (NPMM), City University of Hong Kong, Hong Kong, China.

[9]Solar Fuels Laboratory, Nanyang Technological University, 50 Nanyang Avenue, Singapore 639798, Singapore.

[10]Energy Research Institute @ Nanyang Technological University, 50 Nanyang Avenue, Singapore 639798, Singapore.

[11]Current address: Beijing Key Laboratory for Magnetoelectric Materials and Devices (BKLMMD), Beijing Innovation Center for Engineering Science and Advanced Technology (BIC-ESAT), Department of Materials Science and Engineering, College of Engineering, Peking University, Beijing 100871, China.

[12]Current address: National Synchrotron Light Source II, Brookhaven National Laboratory, 743 Brookhaven Avenue, Building 743, Upton, NY 11973, USA.

*Corresponding author. Email: xuzc@ntu.edu.sg

[Δ]These authors contributed equally to this work.

Abstract

Spinel oxides have attracted growing interest over the years for catalysing the oxygen evolution reaction (OER) due to their efficiency and cost-effectiveness, but the fundamental understanding of the structure-property relationships remains elusive. Here we demonstrate that the OER activity on spinel oxides is intrinsically dominated by the covalency competition between tetrahedral and octahedral sites. The competition fabricates an asymmetric M_T−O−M_O backbone where the bond with weaker metal-oxygen covalency determines the exposure of cation sites and therefore the activity. Driven by this finding, a dataset with more than 300 spinel oxides is computed and used to train a machine learning model for screening the covalency competition in spinel oxides, with a mean absolute error of 0.05 eV. $[Mn]_T[Al_{0.5}Mn_{1.5}]_OO_4$ is predicted to be a highly active OER catalyst and subsequent experimental results confirm its superior activity. This work sets mechanistic principles of spinel oxides for water oxidation, which may be extendable to other applications.

Introduction

The rise in global energy consumption brings increasing demand for the development of a sustainable and clean energy infrastructure.[1,2] Hydrogen gas, which can be produced from water electrocatalysis, is considered as an ideal energy carrier due to its high energy density and cleanliness.[3] However, the overall water splitting suffers from the sluggish oxygen evolution reaction (OER) at the anode, which makes the development of efficient OER catalyst a critical effort.[4,5] Ideally, remarkable OER catalyst should fulfil the requirements as both catalytically active and economically feasible.[6-8] Transition metal spinel oxides (AB_2O_4), where A^{2+} and B^{3+} cations respectively occupy the tetrahedral and octahedral sites, have attracted substantial attention due to their abundance and cost-effectiveness.[9-11] To raise the

OER activity of spinel oxides, tremendous efforts have been spent. For example, substituting some Co by Fe in $ZnCo_2O_4$ ($ZnFe_xCo_{2-x}O_4$) is found to promote the OER activity over $ZnCo_2O_4$, as the injection/extraction of electrons from oxygen is facilitated by Fe substitutes.[12] Duan et al. have incorporated Ni with Co in the octahedral sites of spinel, the constructed $ZnNi_xCo_{2-x}O_4$ (x = 0.6, 0.8) possesses activated lattice oxygen, which gives rise to continuously formed oxyhydroxide as surface-active species and thus enhanced activity.[13] Despite several successful attempts, the reported strategies to date only apply to respective and narrow groups of spinel oxides. To promote more rational screen and design of splendid OER catalysts, a universal principle is required for spinel oxides because of their broad compositional diversity. To establish such principle, a fundamental understanding elucidating the structure-property relationship of OER on spinel oxides is essential and critical.

A well-defined structure-property relationship of OER on transition-metal oxides (TMO) has been established by Alexis Grimaud et al., where the activity of perovskite oxides is described by the bulk O-2*p* band center.[14] The finding highlights the rationality of bridging the OER activity of TMO with their bulk thermochemistry. More recently, study on the lattice oxygen-participated mechanism of OER on perovskites has demonstrated the dominancy of bulk metal-oxygen covalency of TMO_6 in determining the reaction kinetics.[15] This provides valuable clues in designing excellent OER catalysts from spinel oxides since they also contain the TMO_6 structural unit as the perovskite oxides do. However, since the AB_2O_4 frame of spinel enables both A and B sites to be resided by transition metals, the co-existence of TMO_4 and TMO_6 produces more challenges in establishing an accurate structure-property relationship.

In this work, employing both computational and experimental methods, we demonstrate the dominant role of the covalency competition between tetrahedral and octahedral sites in determining the OER activity of spinel oxides. After analysing dozens of reported spinels, a

volcano plot bridging the OER activity and bulk structural parameter is established. Furthermore, we compute and generate a dataset of more than 300 spinels, based on which a machine-leaning assisted approach is employed for ultrafast and accurate covalency prediction. Our machine-leaning model shows only 0.05 eV mean absolute error for screening the covalency competition in spinels. Using this approach, a spinel oxide with outstanding OER activity has been designed and its activity is confirmed by subsequent experiments. Our findings elucidate a comprehensive structure-property relationship of OER on spinel oxides. The electronic database and the machine-learning model developed here may be extendable for developing spinel oxides for other applications.

Results

Relationship between structure property and reaction mechanism

Bulk spinel oxide shows Fd3m space group, with each oxygen atom connected to one tetrahedral cation and three octahedral cations (Figure 1a). Within the structure, tetragonal and octahedral cations are respectively surrounded by four and six negatively charged oxygen, producing repulsive force to the electrons of cations. This repulsive effect, known as the Madelung potential, is determined by the crystallography and is evaluated by summing the electrostatic interactions q^2/r, where q and r stand for the charge and interatomic distance, respectively.[16] Conversely, the electronic energy of oxygen anions is stabilized by the surrounding positively charged metal cations. Due to the crystal field effect, the static electric field splits the *d*-orbitals of the tetrahedral cation into two low-lying e orbitals and three high-lying t_2 orbitals, and the *d*-orbitals of the octahedral cation into three low-lying t_{2g} orbitals and two high-lying e_g orbitals (Supplementary Figure 1). The split *d*-orbitals in each cation contribute together to the narrow *d*-band, which ionically or covalently interacts with the

broad oxygen *p*-band, giving the spinel oxide structure.[17] Specifically, both metals in tetrahedral and octahedral sites have electrons spatially overlapping with the oxygen orbitals, forming σ- and π-bonding MO states and antibonding MO* states. Moreover, as three metal cations (each having five *d* orbitals) and four oxygens (each having three 2*p* orbitals) are incorporated in spinel AB_2O_4, some oxygen orbitals may not hybridize with metallic states, depending on the symmetry or components of the structure (i.e. when Li, Al or Mg is contained), forming non-bonding and purely oxygen *p* states (Figure 1b). These states finally constitute an extended 3D crystal bands that can be integrated to obtain a density of states (DOS) diagram, representing the electronic density for each state in a projective view.

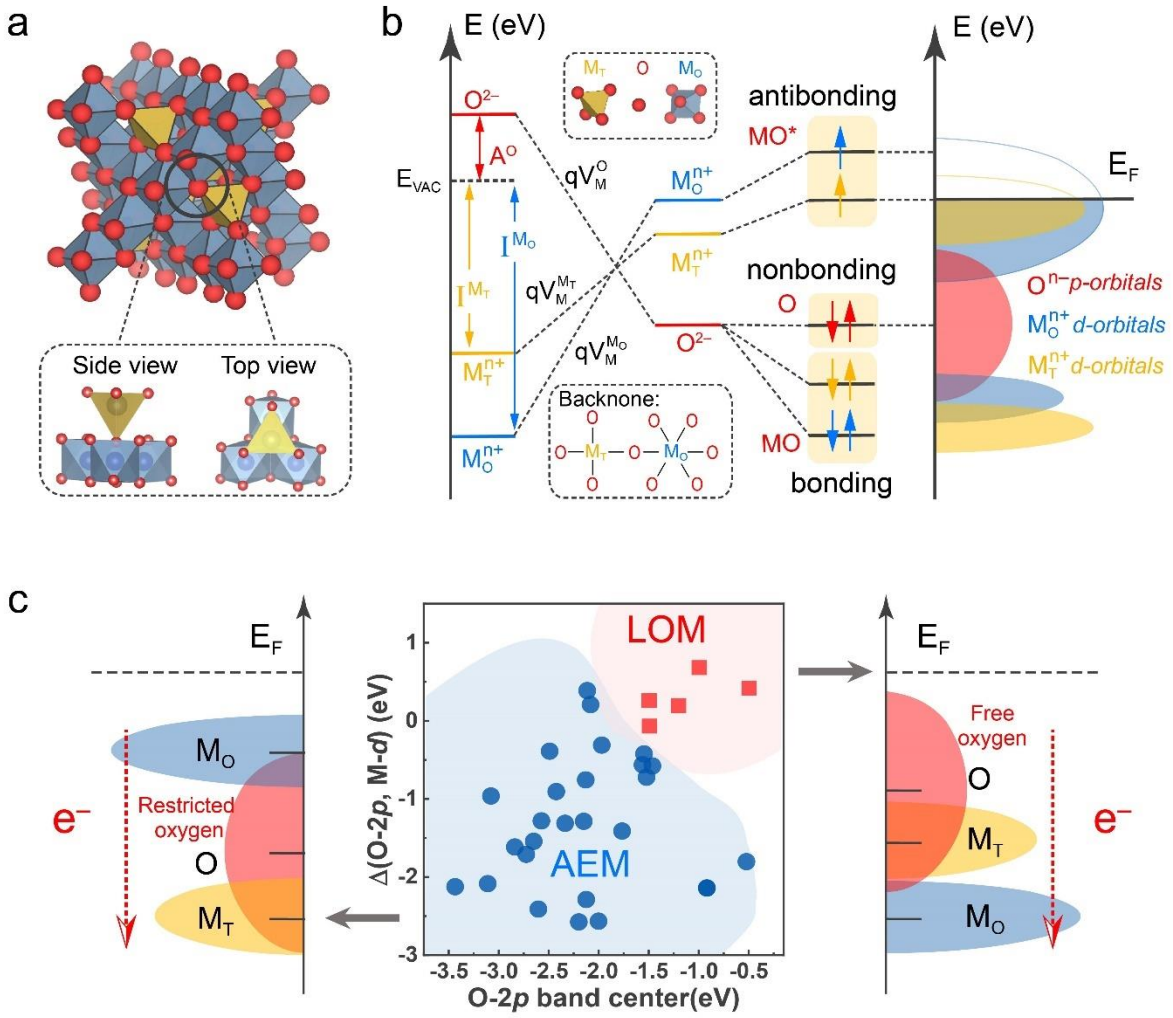

Figure 1 | Patterning OER mechanisms on spinel oxides based on the density of states (DOS). a, Crystal structure of spinel oxide. The polyhedral in orange and blue represents cations in tetrahedral and octahedral sites, respectively. The atoms in red depict oxygen anions. The lower box illustrates the side view and top view of the primitive unit of spinel, where one tetrahedral cation and three octahedral cations are connected to one oxygen anion. **b**, Formation of a density of states (DOS) for spinel oxide with the contributions from tetragonal cations (M_T), octahedral cations (M_O) and oxygen anions (O). The formation originates from the ionization energy of metal cations (I^M) as well as the electron affinity of oxygen (A^O). The symbol q and V represent the charge and Madelung potential, respectively. The crystal interaction gives rise to antibonding MO*, purely oxygen non-bonding O states, and bonding MO orbitals, which finally compose in an extended 3D crystal bands that can be integrated to obtain a DOS diagram, representing the electronic density for each state in a projective view. **c**, Illustration of how the O-2*p* band center and the relative band centers between O-2*p* and active M-*d* co-regulate the reaction mechanism of OER on spinel oxides. For spinels where the energy level of oxygen *p*-band center is low or oxygen is less active than metal cations, the lattice oxygen is firmly restricted and the adsorbates evolution mechanism (AEM) dominants. For spinels whose oxygen *p*-band center is high (e.g. more than −1.75 eV) and is higher than or close to the cation *d*-band center, the lattice oxygen has higher degree of freedom and the lattice oxygen-participated mechanism (LOM) is likely to occur. The experimental reaction mechanisms are referenced from reported works[12,13,18], and unpublished works (Supplementary Table 1). The band centers of spinel oxides are calculated through density functional theory (DFT) calculations (Supplementary Table 1).

It is known that OER could occur via two distinct mechanisms, the adsorbate evolution mechanism (AEM) and the lattice oxygen mechanism (LOM).[19] In the former case, the

reactant (OH^-) donates electrons at the anode surface and evolves to generate oxygen gas via *OH, *O, *OOH, and * (or *OO) intermediates bound to the surface active sites; while in the latter one, lattice oxygen participates in the reaction cycle and becomes part of the gaseous products (Supplementary Figure 2). To be involved in the OER cycle, the lattice oxygen must be active enough to escape from the lattice and segregate to interact with the adsorbed oxygen (*O), which is generated elsewhere during the cycle, leaving a ligand hole (vacancy) in the lattice to be a new active site.

On the other hand, as bias exists, intra-lattice charge transfer occurs during the electrochemical process, which could lead to local charge redistribution.[20] Energetically, in terms of the relative position between oxygen and metal cations, two possible conditions exist in bulk spinel. When oxygen exhibits lower energy level than metal cations (tetrahedral or octahedral), electron transfers from metal cations to oxygen during electrochemical reaction, which constrains the oxygen inside the lattice and blocks the escape and segregation of the lattice oxygen. However, when the band center of oxygen lies above both cations, the closer position of O-2*p* band center relative to the Fermi level might force the electrons flow from oxygen to the nearby cations, which reduces the charges on oxygen. The reduced oxygen has higher degrees of freedom and thus is facile to get released from the lattice. Therefore, to define the reaction mechanism from the electronic point of view, both the absolute energy level of bulk oxygen *p*-band and the relative energy level between oxygen *p*-band and metal *d*-band should be evaluated. Figure 1c illustrates the calculated O-2*p* band center and the energy difference between O-2*p* and metal-3*d* band center (here the metal represents the more active one between octahedral and tetrahedral cations) in more than 30 spinel oxides whose OER reaction mechanisms have been investigated[12,13,18]. As illustrated, spinels exhibiting AEM mechanism and LOM mechanism respectively stay in the top right and bottom left domain, suggesting two distinguishable energetical features. The lattice oxygen in

LOM spinels satisfy both the activity and priority criteria; that is, the O-2*p* band center is considerably high (more than −1.75 eV), which guarantees the possibility of escaping from the lattice, and the oxygen *p*-band level is higher than both cations, which results in the intra-molecular charge transfer from oxygen to cations and reduces the charge on oxygen. Thus, the oxygen *p*-band center and the relative center between oxygen *p*-band and metal *d*-band concurrently regulate the reaction mechanism of OER. Making full use of the dual-parameter, the reaction mechanism of OER on a given spinel oxide can be effectively foreseen. Meanwhile, we believe this dual-parameter can be also used to predict spinel oxides that are not stable and exhibit phase separation, which will need sufficient experimental validations in future.

Covalency competition between tetrahedral and octahedral sites in determining OER activity

In the AB_2O_4 spinel framework, cations in both the tetrahedral and octahedral sites can be covalently bound to oxygen anions (Figure 2a). The formed two types of bond, M_T−O and M_O−O, are generated from the orbital overlap between the metal *d*-orbitals (or *p*-orbitals, e.g. for Al and Mg) and oxygen *p*-orbitals.[17] Since each oxygen is shared by both tetrahedral and octahedral cations, covalency competition exists between the tetrahedral and octahedral cations for overlapping with the full oxygen *p*-orbitals (denoted as M_T−M_O competition), resulting in asymmetrical M_T−O−M_O backbone, in which either M_T−O or M_O−O is weaker. Under OER conditions, where bias exists, the surface structural rearrangement of spinel oxides may occur and bond break is considerably possible at the weaker bond in M_T−O−M_O backbone. In this process, the weaker bond breaks, either M_T−O or M_O−O, leaving the M_T−O−M_O backbone being divided into two counterparts, M−O and M−. The cations in M−O are still fully-coordinated and thus contribute rarely to the reaction performance. The

barely exposed metals (M−), if having unpaired valence electrons, should serve as active sites to adsorb one solvated OH^-, generating M−OH species (the first elementary step in OER cycle, Figure 2a) to start a OER cycle. That is, the break of either M_T−O or M_O−O in the M_T−O−M_O backbone can create exposed metal sites that can be involved in the reaction cycle.

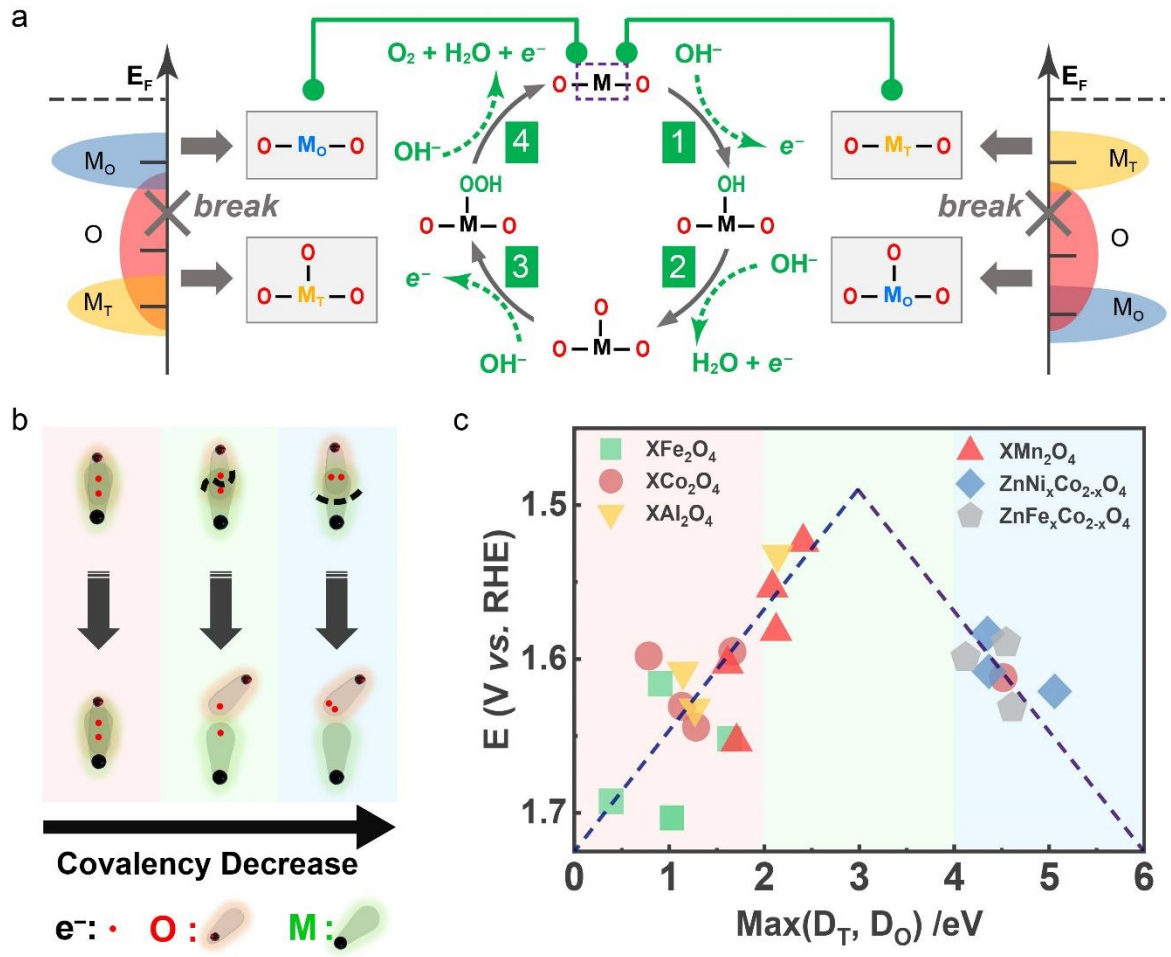

Figure 2 | Relationship between OER activity and the covalency competition in spinel oxides. a, Illustration of how the covalency competition between tetrahedral and octahedral cations in overlapping with oxygen *p*-orbitals (M_T−M_O competition) results in an asymmetrical M_T−O−M_O backbone. And how the two components generated from the break of M−O bond participate in the reaction cycle. **b**, The three possible bond break situations according to different metal-oxygen covalency. For strong M−O covalency (short distance between metal band center and oxygen band center, the pink domain), the bond is difficult to

break. For weak M−O covalency (the blue domain), the bond break will end up with two (partially) ionic parts due to the high polarity. For intermediate M−O covalency (the green domain), bond break will result in the exposure of metal with free radicals. Note that the bond break in spinel structure takes place at the weaker one in M_O−O−M_T backbone, thus either M_T−O or M_O−O can break, depending on which one is weaker. **c**, The experimentally observed reaction activity at as a function of the calculated Max(D_T, D_O) (eV), where D_T represents the distance between the centres of tetrahedral metal *d*-band and oxygen *p*-band and D_O refers to the distance between the centres of octahedral metal *d*-band and oxygen *p*-band. The experimental activity is defined as the potential (V *vs.* RHE) at a given specific current density, i.e., 25 μA/cm^2_{ox} for OER. All the experimental data are taken from published papers[12,13,18] and unpublished works. The details including the potential at 25 μA/cm^2_{ox} (V *vs.* RHE), the simulated compositions, and the calculated Max(D_T, D_O) (eV) are summarised in Supplementary Table 2.

Since starting OER needs the metal cations on surface to react with hydroxyl groups, creating exposed cations is important in promoting the performance of a catalyst.[21] We may hypothesize that the difficulty in breaking the M−O bond of a spinel, which gives rise to exposed metal sites that can immediately take part in the OER cycle, can be directly correlated to its initial reaction performance (at low overpotential or low current). To quantitatively describe the possibility of breaking the M−O bond, the covalency obtained from projected DOS is used to correlate the experimentally observed OER activity (potential (*vs.* RHE) at 25μA/cm^2_{ox}). The covalency is quantified by the distance between the centres of metal *d*-band and oxygen *p*-band (denoted as D_M with the unit of eV). A higher value of D_M indicates a weaker M−O covalency, and thus an easier bond break for active sites creation. In spinel the M−O break occurs at the one exhibiting a weaker M−O covalency in M_O−O−M_T

backbone, the higher D_M between D_T and D_O (denoted as Max(D_T, D_O), where D_T represents the covalency between tetrahedral cations and oxygen, and D_O the covalency between octahedral cations and oxygen) is therefore used to correlate the OER activity (potential at 25 $\mu A/cm^2_{ox}$).

After analysing dozens of the reported spinel oxides[12,13,18], their OER activity as a function of the calculated Max(D_T, D_O) was constructed, which displays a volcano-like shape (Figure 2b). Spinel oxides in the very left side of the volcano graph exhibit strong covalency for both M−O bonds, which makes them difficult (or impossible) to generate active sites and thus exhibit a low OER activity. While for those staying at the very right part of the volcano, they have at least one M−O bond with quite low covalency, suggesting an easy bond-break. However, the low covalency intrinsically suggests highly polar chemical bond, where the electrons forming the bond are unequally distributed. In this case, the bond break will result in formation of two ionic components, which have no unpaired electrons and hence can hardly be active to adsorb hydroxyl groups for next OER. Alternatively, if staying at the middle part of the volcano, the bond is neither too strong nor too polarized. When bias is applied, the bond has high possibility to break. Also, as the polarity is not high enough for ions formation, the bond break will end up with an equal distribution of the shared electron pairs between metal and oxygen, resulting in metals with unpaired electrons exposed, which can act as actives sites in the reaction cycle and contribute to the OER performance. In other words, to generate active sites, two conditions need to be satisfied. First, the M−O bond should not be too strong, which guarantees the bond break under electrochemical conditions. Secondly, the bond should not be too polarized, which enables the formation of exposed metals with unpaired electrons rather than ions. The peak of the volcano is located around 3 eV, indicating that spinels with a 3 eV value of Max(D_T, D_O) are excellent candidates for catalysing OER. It is worth mentioning that it is the AB_2O_4 framework of spinel oxide that

makes the M_T−M_O competition crucial in determining the OER activity, since all the other factors discovered based on perovskite oxides, such as O-2*p* band center[14,22], bulk oxygen vacancy formation energy[22], e_g occupation of TMO_6 structural unit[23], and single M−O covalency[15], are found not universally applicable to the experimental results of all reported spinel oxides to date (Supplementary Figure 3). In perovskite ABO_3 frame, the A sites are normally resided by alkaline or rare-earth metals and their contributions to OER are relatively insignificant. Thus, a rational elucidation of B site cations or B–O covalency is sufficient to describe OER on perovskites. However, the spinel AB_2O_4 frame allows both A and B sites to be resided by transition metals, which implies both tetrahedral and octahedral cations could take part in the OER cycle. To set up a universal design principle, the chemical features of A–O and B–O both need to be considered. This defines the principal distinction between perovskites and spinels, which ultimately makes the covalency competition between tetrahedral and octahedral sites critical in determining the OER activity. Besides, the covalency competition theory established here may also provide clues to explain the catalytic activity on other types of materials, where multiple catalytic sites exist.

Machine-learning approach for fast screening the covalency competition in spinel oxides

Although the nature of spinel M_T−M_O competition in determining the OER activity has been unveiled, the summit of the volcano remains vacant. To deeply explore the potential of spinels in oxygen electrocatalysis and find out a benchmark spinel oxide, we calculate and generate a comprehensive dataset with more than 300 spinels, where normal, (partially) inversed, metal substituted, and defective compositions have all been considered. As shown in Figure 3a, most of the calculated spinels locate in the top-left of the panel, indicating octahedral cation tends to bind oxygen more tightly than tetrahedral cation. Among the

screened spinels, only a few with tetrahedral Zn and Li have the D_T ranging from 4 eV to 6 eV, suggesting the possible utility of these two cations in weakening the metal-oxygen covalency. Inspiringly, plentiful spinel oxides estimate top-class OER activity, as their Max(D_T, D_O) are close to the optimal level (the red dots). Thus, theoretically, spinel oxides are an ideal class of materials for catalysing OER. As this work utilizes the bulk thermochemistry to describe the OER activity, the solvation model that addresses the role of electrolyte to the solid/liquid interface is not included. It's worth noting that the OER activities of some materials are reported to exhibit dependence to the change of the cationic species[24-26] and pH value[12,15] of the electrolyte. However, since the function of electrolyte is to influence the thermodynamics and kinetics at the catalyst/electrolyte interface, although the absolute activity may evolve with the change of electrolyte, the relative trend should most likely remain the same.

After obtaining the dataset, we apply statistical and machine-learning (ML) techniques (more details are summarised in Method, Supplementary Table 7, Supplementary Figure 4, and Supplementary Figure 5) to screen the covalency competition in spinel oxides.[27] To make the screening precise and accurate, the feature-based approach is employed, where the elemental and structural features of spinel are both considered. Elementally, the atomic radius, number of valence electrons, and the cut-off energy for plane wave basis are coded to describe anions and cations (the sets are detailed in Supplementary Table 7). Structurally, as two types of cations co-exist in spinel lattice, the tetrahedral and octahedral sites are described individually. In AB_2O_4 lattice, if all the octahedral sites are empty and only the tetrahedral sites are filled, the crystal has the zinc-blende structure; while if only octahedral sites are occupied, the crystal exhibits the rock-salt structure.[17] Thus, to simplify, the spinel lattice may be thought of as an ordered mixture of the zinc-blende and rock-salt structure. It is therefore expected that the metal-oxygen covalency in zinc-blende and rock-salt can be used

to describe the structural feature of spinels. Considering both the elemental and structural features, a machine-learning model, denoted as covalency competition model, is established using the random forest algorithm (Figure 3b). The verification of ML algorithm was performed by analyzing the mean absolute error (MAE). The MAE of the predicted Max(D_T, D_O) from this model is only 0.05 eV, indicating the data predicted by the model match closely with those calculated from DFT. By contrast, the MAE from the model where the data are trained without the structural feature is considerably higher, with the value to be 0.09 eV (Supplementary Figure 6). This provides direct indication of the mathematical correlation between the covalency in spinel and that in zinc-blende and rock-salt structure. When crystalizing a spinel structure, oxygen is no longer bound to one single type of cations, but shared simultaneously by tetrahedral and octahedral cations. The competition between these two types of cations in overlapping with the oxygen *p*-orbitals exists in the M_O−O−M_T backbone, which finally contributes and shapes the whole covalency pattern in spinel oxides. With the establishment of covalency competition ML model, both the reaction mechanism and the covalency competition in spinels can be ultrafast predicted.

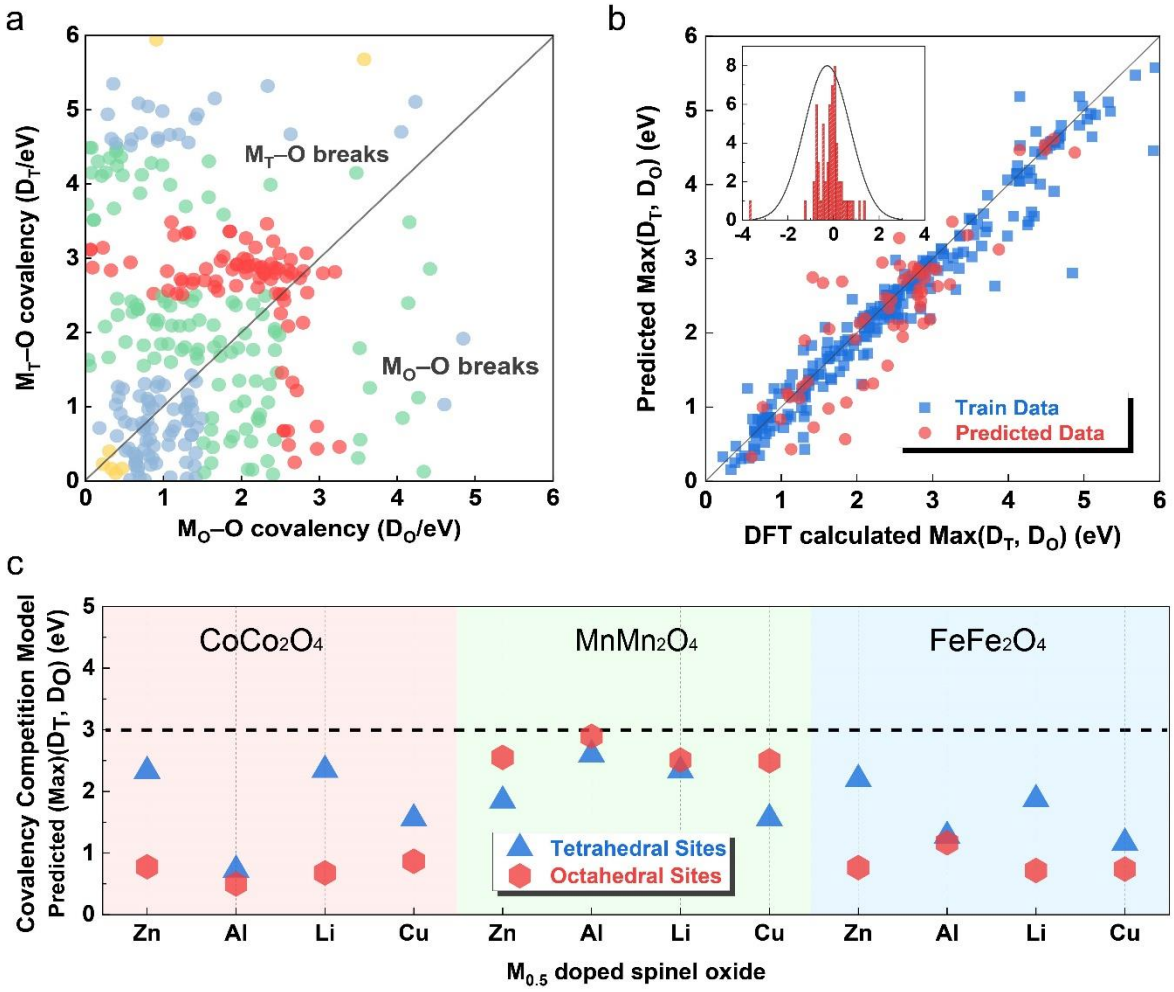

Figure 3 | Machine learning approach for fast screening the covalency competition in spinel oxides. a. The calculated electronic dataset of more than 300 spinel oxides. The *x*-axis and *y*-axis present the M_O–O covalency (D_O) and M_T–O covalency (D_T), respectively. The dots in red represent the covalency in the range of 2.5 eV to 3.5 eV. The dots in green represent those with the covalency in the range of 1.5 eV to 2.5 eV and 3.5 eV to 4.5 eV. The dots in blue represent those with the covalency in the range of 0.5 eV to 1.5 eV and 4.5 eV to 5.5 eV. The dots in yellow represent those with the covalency in the range of 0 eV to 0.5 eV and 5.5 eV to 6 eV. Of all the screened spinels, only those with both D_T and D_O ranging from 0 eV to 6 eV are shown. The detailed structural composition and metal-oxygen covalency of the dataset can be found in Supplementary Table 3–6. **b**. The established machine-learning model (covalency competition model) for screening the covalency competition in spinel

oxides. The dots in blue and red denote the training points and predicted points, respectively. The *x*-axis in the insert box shows the deviation between the covalency competition model predicted Max(D_T, D_O) and DFT calculated Max(D_T, D_O). The *y*-axis in the insert box represents the counts of the dots. The feature sets are summarized in Supplementary Table 7. **c**. The predicted Max(D_T, D_O) of $M_{0.5}$ (M = Zn, Al, Li, and Cu) substituted $CoCo_2O_4$, $MnMn_2O_4$, and $FeFe_2O_4$ by the covalency competition model. The blue and red dots denote spinel $[M_{0.5}Mn_{0.5}]_T[Mn_2]_OO_4$ and $[Mn]_T[M_{0.5}Mn_{1.5}]_OO_4$, respectively.

Using the covalency competition model, several spinel oxides composed by earth-abundant elements have been screened and their Max(D_T, D_O) are generated. Specifically, we have used $M_{0.5}$ (M = Zn, Al, Li, and Cu) to substitute the cations in $CoCo_2O_4$, $MnMn_2O_4$, and $FeFe_2O_4$. As shown in Figure 3c, depending on the cation's substitution site – tetrahedral or octahedral, completely different metal-oxygen covalency are obtained, suggesting controlling the substitution site is a practicable strategy in manipulating the covalency in spinel. Among the screened candidates, spinel $[Mn]_T[Cu_{0.5}Mn_{1.5}]_OO_4$, $[Mn]_T[Al_{0.5}Mn_{1.5}]_OO_4$, and $[Mn]_T[Zn_{0.5}Mn_{1.5}]_OO_4$ have their Max(D_T, D_O) values predicted by the covalency competition model close to the optimal value, estimating good OER activity. However, as Cu and Zn generally exhibit +2 valence state in oxide and situate in the tetrahedral sites,[18,28] difficulties may exist in synthesizing the matching structure experimentally. By contrast, metal Al typically shows +3 valence state and usually takes the octahedral sites in spinel structure.[29] Thus, predicted spinel $[Mn]_T[Al_{0.5}Mn_{1.5}]_OO_4$ should be a promising highly active and experimentally feasible catalyst.

Synthesis, characterization, and OER activity of $[Mn]_T[Al_{0.5}Mn_{1.5}]_OO_4$

To confirm the OER performance of the as-predicted Al substituted $MnMn_2O_4$, spinel $Al_{0.5}Mn_{2.5}O_4$ was synthesized and characterized. As shown in Figure 4a, the energy-dispersive X-ray spectroscopy (EDS) illustrates that Mn and Al distribute evenly in the oxide, implying the crystallization of aluminium, manganese, and oxygen in spinel $Al_{0.5}Mn_{2.5}O_4$. The high-angle annular dark-field (HAADF) scanning transmission electron microscopy (STEM) image in Figure 4b shows a lattice direction of [001] and [110]. From the bottom-right pattern, it can be obviously seen that each oxygen in spinel lattice is shared by three octahedral cations and one tetrahedral cation. The X-ray diffraction (XRD) pattern (Figure 4c) of the as-synthesized oxide indicates a typical tetragonal spinel structure. The observed peaks at around 18.0°, 28.9°, 32.3°, 36.1°, and 59.8° respectively correspond to the (101), (112), (103), (211), and (224) lattice planes of $MnMn_2O_4$ (PDF#24-0734). When Al substitutes Mn in $MnMn_2O_4$ lattice, all the diffraction peaks show a slight right-shift. That is due to the lattice shrinkage caused by the partial replacement of Mn atoms by Al with a smaller radius.[30] All the above results indicate that the structure of $Al_{0.5}Mn_{2.5}O_4$ remains in a spinel frame.

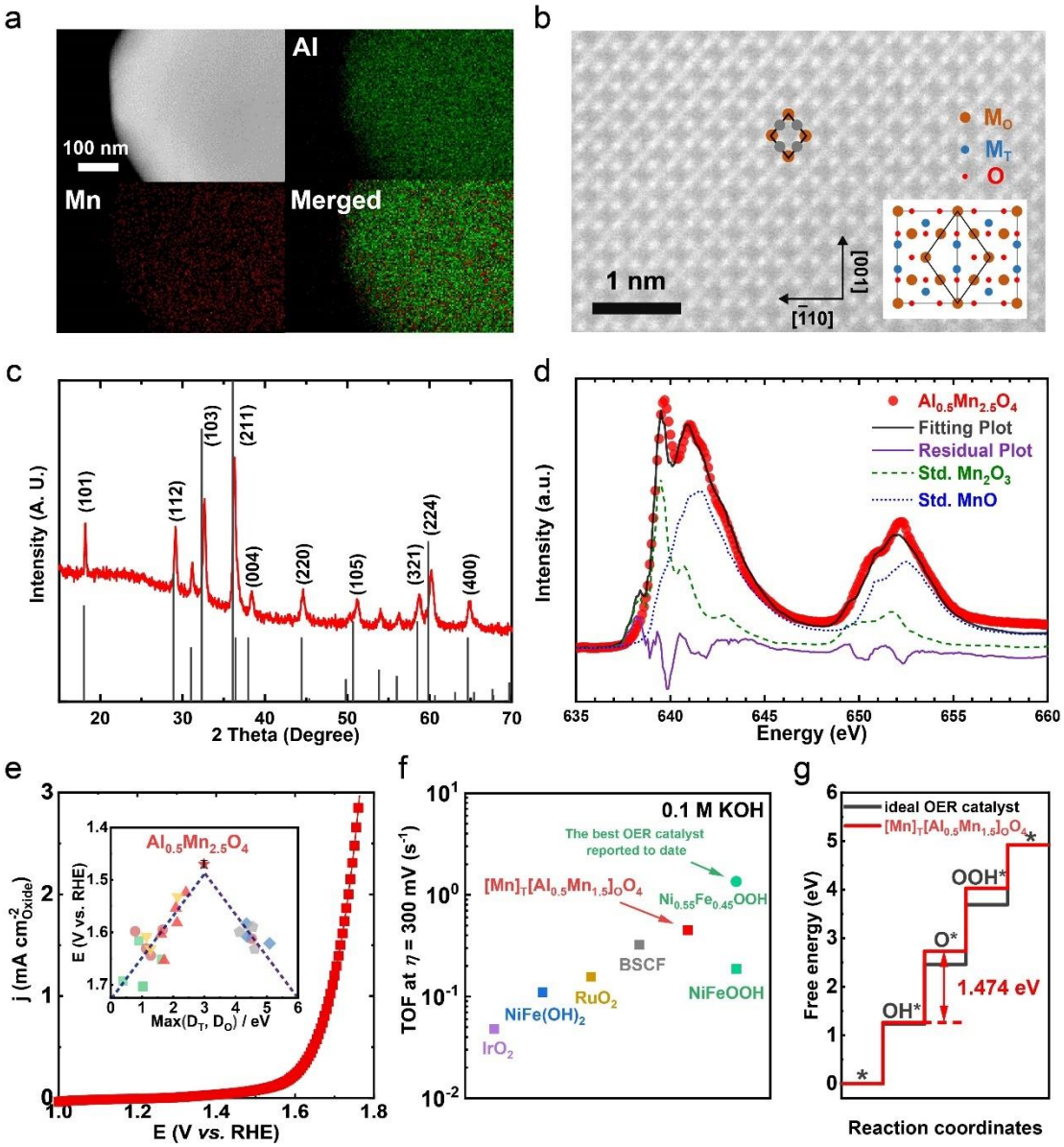

Figure 4 | Experimental analysis of the synthesized spinel $Al_{0.5}Mn_{2.5}O_4$. a. Energy-dispersive X-ray spectroscopy (EDS) elemental mapping of spinel $Al_{0.5}Mn_{2.5}O_4$. **b.** The high-angle annular dark-field (HAADF) scanning transmission electron microscopy (STEM) image of the as-synthesized $Al_{0.5}Mn_{2.5}O_4$. **c.** The X-ray diffraction (XRD) pattern of the as-synthesized spinel $Al_{0.5}Mn_{2.5}O_4$. **d.** Linear combination fitting for the Mn $L_{2,3}$-edge X-ray absorption spectrum (XAS) of the as-synthesized $Al_{0.5}Mn_{2.5}O_4$, using MnO and Mn_2O_3 as reference samples. **e.** iR-corrected linear sweep voltammogram (LSV) curves of the as-synthesized $Al_{0.5}Mn_{2.5}O_4$ oxide. The raw LSV data are shown in Supplementary Figure 9.

The inset box illustrates the location of $Al_{0.5}Mn_{2.5}O_4$ in the constructed volcano plot. Error bar was obtained by repeating the electrochemical test for three times. **f.** Turnover frequency (TOF) of the as-synthesized $Al_{0.5}Mn_{2.5}O_4$ and other reference OER catalysts in 0.1 M KOH. The red dot shows the TOF of $Al_{0.5}Mn_{2.5}O_4$. The purple dot shows the TOF of IrO_2 calculated based on the data from the work by K. A. Stoerzinger et al.[37]. The blue dot shows the TOF of $NiFe(OH)_2$ synthesized in this work. The TOF value of RuO_2 and $Ba_{0.5}Sr_{0.5}Co_{0.8}Fe_{0.2}O_{3-\delta}$ (BSCF) are directly taken from the work by W. T. Hong et al.[38]. The green dots illustrate the TOF of $Ni_aFe_{1-a}OOH$ calculated based on data from reported works. The lower one is the average performance of NiFeOOH from the work by O. Diaz-Morales et al.[39]. The upper one is the TOF of $Ni_{0.55}Fe_{0.45}OOH$ from the work by M. Görlin et al.[40], which is the best OER catalyst in 0.1 M KOH reported to date. The synthesis, characterizations and OER measurement of $NiFe(OH)_2$ are detailed in Method. The procedures of TOF calculations are detailed in Equation 3-14. **g.** The DFT calculated OER free energy diagram on the most close-packed surface of $[Mn]_T[Al_{0.5}Mn_{1.5}]_OO_4$ oxide. Tetrahedral Mn is considered as the active site. The pathway on an ideal catalyst is also shown as reference.

To probe the valence and occupation state of Mn in the spinel oxide, X-ray absorption near-edge spectroscopy (XANES) of Mn *K* and $L_{2,3}$-edge were collected.[31] The Mn *K*-edge XANES (Supplementary Figure 7) shows the Mn valence state of $Al_{0.5}Mn_{2.5}O_4$ is between that of MnO and Mn_3O_4, which qualitatively implies that Al mainly locates in the octahedral sites, as Mn^{2+} prefers to occupy the tetrahedral interstices while Mn^{3+} tends to occupy the octahedral interstices.[10] To quantitatively obtain the Mn occupation in $Al_{0.5}Mn_{2.5}O_4$, we have performed the $L_{2,3}$-edge XAS linear combination fitting, using MnO and Mn_2O_3 as reference samples (Figure 4d).[32] The fitting results suggest almost all the Al atoms reside in the octahedral sites, implying a chemical formula of $[Mn]_T[Al_{0.5}Mn_{1.5}]_OO_4$ for spinel

$Al_{0.5}Mn_{2.5}O_4$ (more details of the Mn occupation fitting can be found in Method, Supplementary Table 8, and Supplementary Figure 8). Subsequent electrochemical measurement was performed within a potential window of 1.0~1.8 V (*vs.* RHE) in 0.1 M KOH, with the catalytic activities being normalized by the surface area of oxides to reflect the intrinsic activity (Figure 4e).[33,34] The surface area of the as-synthesized spinel was determined by Brunauer–Emmett–Teller (BET) measurements, which is considered rational for measuring metal oxide catalysts.[34-36] As shown in Figure 4e, at the current density of 25 $\mu A/cm^2_{ox}$, the potential of OER on spinel $[Mn]_T[Al_{0.5}Mn_{1.5}]_OO_4$ is characterized to be 1.47 V (*vs.* RHE), i.e. an overpotential of 240 mV. With reference to the established volcano plot, spinel $[Mn]_T[Al_{0.5}Mn_{1.5}]_OO_4$ locates at the summit of the volcano, indicating remarkable activity for OER (insert box in Figure 4e). It's worth noting that the inductively coupled plasma (ICP, Supplementary Table 11) and line scan (Supplementary Figure 10) results suggest Al is partially leached out into the solution; however, HRTEM study of the samples before and after long-time OER cycling (Supplementary Figure 10) revealed no surface reconstruction to amorphous or hydroxides structures occur, indicating the exhibited activity is still attributed to the oxide in spinel frame. What's more, spinel $[Mn]_T[Al_{0.5}Mn_{1.5}]_OO_4$ with partial Al vacancies are also remarkable OER catalysts, as their predicted $Max(D_T, D_O)$ are close to the optimal value of 3 eV (Supplementary Figure 11). The stability tests (over 1000 cycles and 12-hour CA) demonstrate a good durability of the as-synthesized spinel under the operating condition (Supplementary Figure 12). The comparison between the intrinsic OER activity of the as-synthesized $[Mn]_T[Al_{0.5}Mn_{1.5}]_OO_4$ and that of the state-of-the-art catalysts[37-40] was thereafter performed (Figure 4f), which further confirms the high intrinsic activity of spinel $[Mn]_T[Al_{0.5}Mn_{1.5}]_OO_4$. The turnover frequency (TOF) is used to represent the intrinsic activity, which was calculated assuming the surface metal atoms are active sites. As illustrated, TOF calculated for $Ni_{0.55}Fe_{0.45}OOH$ is 1.35 s^{-1}, which is to date the best reported

OER catalyst in 0.1 M KOH.[40] For spinel $[Mn]_T[Al_{0.5}Mn_{1.5}]_OO_4$, the calculated TOF is 0.45 s^{-1}, indicating slightly poorer activity than the benchmark $Ni_{0.55}Fe_{0.45}OOH$; however, its TOF is higher than many of the other reference catalysts, including IrO_2[37], $NiFe(OH)_2$, RuO_2[38], and the perovskite $Ba_{0.5}Sr_{0.5}Co_{0.8}Fe_{0.2}O_{3-\delta}$ (BSCF)[38]. Finally, the free energy diagram of OER on the tetrahedral Mn was calculated. As shown in Figure 4g, the overpotential on spinel $[Mn]_T[Al_{0.5}Mn_{1.5}]_OO_4$ is mainly resulted from the inadequate adsorption energy of *OH and *OOH, which stay above the level of an ideal catalyst.[41] To initiate the reaction, a 1.474 eV uphill free energy needs to be surmounted to make the rate-determining step of *OH to *O ($*OH + OH^- \rightarrow *O + H_2O$) a thermally neutral process, estimating a 1.474 V (*vs.* RHE) reaction potential. Therefore, the superior OER activity of the as-predicted $[Mn]_T[Al_{0.5}Mn_{1.5}]_OO_4$ is experimentally confirmed.

Conclusions

In summary, employing both computational and experimental approaches, we describe how the OER mechanism and activity on spinel oxides can be associated with their bulk electronic structure. The OER mechanism on spinel is demonstrated to be concurrently determined by the oxygen *p*-band centre and the relative reactivity between oxygen *p*-band and metal *d*-band. The OER activity originates from the covalency competition between tetrahedral and octahedral cations for overlapping with oxygen *p*-orbitals (M_T–M_O competition), which results in an asymmetric M_O–O–M_T backbone and regulates the exposure of active catalysis sites. The ability of M_O–O–M_T break is found to volcanically relate to OER activity. A machine-learning enabled mathematical approach was further developed for ultrafast covalency competition screening. The established covalency competition model provides the covalency competition result in spinel with the mean absolute error of only 0.05 eV. The approach predicted spinel $[Mn]_T[Al_{0.5}Mn_{1.5}]_OO_4$ to be an outstanding electrocatalyst for OER. Subsequent experiments validated the OER activity of the as-designed spinel, which exhibits

only 240 mV (*vs.* RHE) overpotential at 25 $\mu A/cm^2_{ox}$. These findings provide comprehensive understanding of oxygen electrocatalysis by spinel oxides and present the related design concepts. Besides, it's worth noting that the covalency competition theory is a universal structure-property relation that applicable to all spinel family, and it best describes those thermodynamically stable spinels that remain AB_2O_4 frame under OER conditions. For those undergoing surface reconstruction to amorphous or hydroxide structures, evaluations on the bulk features that induce the surface reconstruction and the thermochemistry of the reconstructed surface are also essential to give a more characteristic description. The mathematical model established here may be extendable to other applications, in which high performance spinel oxides are needed.

Methods

Density functional theory (DFT) calculations. All the spin-polarized density functional theory (DFT) calculations were performed with the Vienna Ab-initio Simulation Package[42,43] (VASP), employing the projector-augmented wave[44] (PAW) model. The exchange and correlation effects were described by Perdew-burke-Ernzerhof[45] (PBE) functional, under the generalized gradient approximation (GGA) approach. The Hubbard U corrections were adopted where transition metals are contained, using the model proposed by Dudarev et al.[46] The U_{eff} (U_{eff} = Coulomb U–exchange J) values of each transition metal were summarized in Supplementary Table 9. In all the cases, the cutoff energy was set to be 450 eV. The bulk structures of spinel oxides were optimised by using 6 × 6 × 6 and 11 × 11 × 6 Monkhorst−Pack[47] k-point mesh for the cubic and tetragonal configurations, respectively. After structure optimization, the projected density of states (PDOS) calculations were carried out by using 9 × 9 × 9 and 15 × 15 × 9 Monkhorst−Pack k-point mesh for cubic and tetragonal spinels, respectively. Of all the calculations, the Brillouin zone was integrated using tetrahedron method with Blöch corrections.[48] The force and energy convergence tolerance were set to be 0.01 eV $Å^{-1}$ and 10^{-5} eV, respectively. For spinels with metal substitutes, the guest cations were arranged as random as possible inside the spinel lattice. The effective O-*p* band center and M-*d* band center were respectively determined by the weighted average of the *p*-band and *d*-band states (both occupied and unoccupied states) from the computed PDOS. The atomic coordinates of the spinels for training the covalency competition model are summarised in Supplementary Data 1. The atomic coordinates of the OER intermediates on spinel $[Mn]_T[Al_{0.5}Mn_{1.5}]_OO_4$ are summarised in Supplementary Data 2. The bulk oxygen formation energy of spinel oxides was calculated as the energy difference between the vacant spinel together with an oxygen atom and the intact spinel structure, which was defined as

$$\Delta E_{vacancy-form} = E_{vacant-bulk} + E_{oxygen} - E_{intact-bulk} \quad (1)$$

where $E_{vacant\text{-}bulk}$, E_{oxygen}, and $E_{intact\text{-}bulk}$ represent the electronic energy of the spinel with one bulk oxygen vacancy, the chemical potential of one oxygen atom referenced to gaseous oxygen molecule, and the electronic energy of the intact spinel, respectively.[22] Under this definition, a lower value of bulk oxygen formation energy suggests an easier case for generating an oxygen vacancy.

Machine learning approach. Machine learning approach was operated based on the DFT calculated data for fast and accurate covalency competition screening. The machine learning process was implemented using the open-source Anaconda Distribution (Python 3.7.3, numpy 1.16.2). The scikit-learn package was used to perform the whole machine leaning approach. The data training and prediction were carried out under the random forest algorithm, which is an effective learning method for both regression and classification.[27,49,50] To describe the structure of spinel AB_2O_4, we have used the following parameters as input features: the stoichiometric number of element in tetrahedral and octahedral sites, the electronegativity of each element, ionic radii of elements in tetrahedral and octahedral sites, valence electron numbers of each element, atomic cutoff radius, and the band centres in zinc-blende and rock-salt structures (Supplementary Table 7). The output includes the band centres of O-2*p*, M_O-*d*, and M_T-*d*. After obtaining these results, the metal-oxygen covalency was then calculated. The detailed machine learning procedures in this work are illustrated in Supplementary Figure 4 and Supplementary Figure 5. The verification of ML algorithm was performed by analyzing the mean absolute error (MAE). The mean absolute error in this work is defined as the average of absolute errors between the covalency competition model

predicted Max(D_T, D_O) and the DFT calculated Max(D_T, D_O). The formula of MAE is as follow:

$$\mathrm{MAE} = \frac{1}{n}\sum_{t=1}^{n}|P_i - C_i| \quad (2)$$

where P_i is the value predicted by covalency competition model, C_i is the value calculated by DFT, and n is the total number of the screened spinels.

Synthesis and characterization of $Al_{0.5}Mn_{2.5}O_4$. Spinel $Al_{0.5}Mn_{2.5}O_4$ was synthesized by a sol-gel combustion method.[51] All chemicals were used as bought without further purification. In the synthesis process, 5 mmol of $Al(NO_3)_3$ (Sigma-Aldrich) and 25 mmol of $Mn(CH_3COO)_2$ (Sigma-Aldrich) were mixed in diluted nitric acid solution (30 ml deionized water + 5 ml nitric acid) by vigorous stirring. Acting as chelating agent, 15 mmol of citric acid (Sigma-Aldrich) was then added in the mixture. After stirring at 90 °C for 9 hours, the mixture solution was converted into viscous gel. The gel was then decomposed in air at 170 °C (the heating rate was set to be 10 °C min^{-1}) for 12 hours to thoroughly remove the remaining water and ground. After applying a further heat treatment in air at 1100 °C (with a heating rate of 5 °C min^{-1}) for 6 hours, phase-pure spinel oxide particles were obtained.

The high-angle annular dark-field (HAADF) scanning transmission electron microscopy (STEM) image was obtained on a JEOL ARM200F (JEOL, Tokyo, Japan) aberration-corrected transmission electron microscope operated at 200 kV with a double hexapole Cs correctors (CEOS GmbH, Heidelberg, Germany) and cold field emission gun. The convergent semiangle of the probe was set at about 30 mrad. The HAADF-STEM image was collected by using a half-angle range from about 68 to 280 mrad. The energy-dispersive X-ray spectroscopy (EDS) was carried out on a JEOL JEM-2100 field emission TEM operated at 200 kV. The crystalline phase of the samples was determined by X-ray diffraction (XRD)

collected on a Bruker D8 powder diffractometer with Cu Kα radiation (λ = 0.15418 nm) operated at 45 kV and 40 mA. The thermogravimetric analysis (TGA) was conducted on a TGA TA Instruments Q500 System under air flow (60 mL·min^{-1}) with a heating rate of 10 °C min^{-1}. The Brunauer–Emmett–Teller (BET) measurements were performed on ASAP Tri-star II 3020 physisorption analyzer at 77 K.

X-ray absorption near-edge spectroscopy (XANES). XANES of Mn *K* edge were collected at X-Ray Absorption Facility for Catalysis Research (XAFCA) beamline of Singapore Synchrotron Light Source.[52] The sample was prepared by compacting the mixture of spinel oxide powders and boron nitride (powder, ~1 μm, 98%, Sigma Aldrich) into pellets. Data reduction and data analysis were performed with the Demeter software package[53]. A normalized absorption ranging from 0.15 ~ 1.00 has been chosen to determine the position of edges. The Mn *K*-edge XANES spectra of the as-synthesized $Al_{0.5}Mn_{2.5}O_4$ and standard samples is shown in Supplementary Figure 6.

***L*$_{2,3}$-edge X-ray absorption spectrum (XAS).** The $L_{2,3}$-edge XAS were collected at the soft X-ray and ultraviolet (SUV) beamline of the Singapore Synchrotron Source[54], which is a compact, 700 MeV electron storage ring that produces synchrotron radiation from two superconducting dipoles having a magnetic flux density of 4.5 T, with a ring circumference of 10.8 m. The Mn $L_{2,3}$-edge spectra were fitted by means of a linear combination analysis, using the spectra of reference manganese oxides for each of the Mn cations, i.e. MnO for Mn^{2+} and Mn_2O_3 for Mn^{3+}. This method has been reported before and proved to provide effective Mn occupation in spinel structure.[32] To test the validation of this fitting approach, we have also fitted Mn occupation of Mn_3O_4 standard sample (Supplementary Figure 7). The

parameters obtained from fitting the Mn $L_{2,3}$-edge XAS are summarized in Supplementary Table 8. The closeness between the obtained Mn_3O_4 parameters and the real Mn occupation in Mn_3O_4 confirms the effectiveness of this fitting method.

Electrochemical measurement of OER activities. The as-synthesized spinel catalyst, acetylene black (AB), and Nafion© solution were mixed through ultrasonication for 2 hours in ethanol to form the uniform catalyst ink. 10 μL of as-prepared ink with the final concentrations of 1.8 mg mL^{-1} oxide, 4.2 mg mL^{-1} AB, and 1 mg mL^{-1} Nafion© were dropped onto the glassy carbon electrode (geometric surface area: 0.196 cm^2). Oxygen electrocatalysis experiments were conducted in O_2-saturated 0.1 M KOH with a Pt counter electrode and a Hg/HgO reference electrode. The scan rate for LSV and CV was kept at 10 mV s^{-1}. All the polarization curves were iR-corrected in regard to the ohmic resistance of the solution. The resistance was measured by electrochemical impedance spectroscopy (EIS) technique. The EIS was performed using AC impedance spectroscopy, with the working electrode biased as a certain potential while the frequency ranged from 100 kHz to 0.01 Hz. Capacitive current was corrected by averaging the forward and backward sweeps.[55] Current density in all the test was normalized to the catalyst surface area, which was determined by BET measurement. The overpotential was calculated as the difference between the reaction potential (at 25 $\mu A/cm^2_{ox}$) and the equilibrium potential (1.23 V).

Synthesis, characterization, and OER measurement of $NiFe(OH)_2$ in this work. The NiFe double hydroxides were prepared by the coprecipitation route, using 0.1 M solutions of $Ni(NO_3)_2$ and $Fe(NO_3)_3$ as precursors. The precipitation was performed at 80 °C. 10 mL water was first adjusted to a pH 9 solution with 0.1 M Na_2CO_3. Solution containing 0.1 M

$Ni(NO_3)_2$ and 0.1 M $Fe(NO_3)_3$ was then slowly added to mix with the previously prepared solution. The pH was kept approximately constant at 9 during the synthesis by simultaneous dropping of 0.1 M Na_2CO_3. The addition of the Ni^{2+}/Fe^{3+} solution (30ml) and the Na_2CO_3 was completed within 1.5 h, after which the suspension was separated by centrifuge at 5000 rpm for 5 mins. The powders were subsequently dried overnight at 120 °C for 2 days and finely grown.

The crystalline structure of the samples was measured by X-ray diffraction (XRD) collected on a Bruker D8 powder diffractometer with Cu Kα radiation (λ = 0.15418 nm) operated at 45 kV and 40 mA. The thermogravimetric analysis (TGA) was conducted on a TGA TA Instruments Q500 System under air flow (60 mL·min^{-1}) with a heating rate of 10 °C min^{-1}. The energy-dispersive X-ray spectroscopy (EDS) was carried out on a FESEM 7600F at 15 kV. The Brunauer–Emmett–Teller (BET) measurements were performed on ASAP Tri-star II 3020 physisorption analyzer at 77 K. The OER measurement procedure of $NiFe(OH)_2$ was the same as that of spinel $[Mn]_T[Al_{0.5}Mn_{1.5}]_OO_4$.

Turnover frequency (TOF) calculation of $[Mn]_T[Al_{0.5}Mn_{1.5}]_OO_4$, $NiFe(OH)_2$ in this work, $Ni_aFe_{1-a}O_xH_y$, IrO_2, RuO_2, and $Ba_{0.5}Sr_{0.5}Co_{0.8}Fe_{0.2}O_{3-\delta}$ (BSCF). The TOF of these catalysts were calculated using the following equation

$$TOF = \frac{j_{BET} \times A_{oxide}}{4 \times e \times N} = \frac{j_{BET}}{4 \times e \times \rho} \quad (3)$$

where j_{BET}, A_{oxide}, N, ρ, and e stands for the BET normalized current density at the overpotential of 300 mV, the surface area of the lattice plane, the number of atoms within the lattice plane, the density of surface metal atoms, and the charge of a single electron, respectively.

$Al_{0.5}Mn_{2.5}O_4$. In order to estimate the number of surface Mn atoms, we have used the surface density of atoms within the (111) plane in the unit cell of $[Mn]_T[Al_{0.5}Mn_{1.5}]_OO_4$. The (111) plane is chosen because it is the most close-packed surface of spinel[56] (with low surface energy) and has the highest cation density[57] (so that the activity will not be overestimated). Based on the crystallographic data, the number of active Mn atoms (N_T, as tetrahedral sites are exposed in this case) and the surface area of the spinel oxide (A_{oxide}) can be determined as

$$N_T = 1 \times 0 + \frac{1}{2} \times 2 + \frac{1}{4} \times 2 = 1.5\ atoms \quad (4)$$

$$A_{(111)} = \frac{\sqrt{2}a}{2} \times \sqrt{\frac{a^2}{2} + c^2} = \frac{\sqrt{2} \times (5.88\ \text{Å})}{2} \times \sqrt{\frac{(5.88\ \text{Å})^2}{2} + (9.59\ \text{Å})^2} = 4.34 \times 10^{-19}\ m^2 \quad (5)$$

Thus, at the overpotential of 300 mV (with the current density to be 0.1 mA/cm^2_{ox}), the TOF of $[Mn]_T[Al_{0.5}Mn_{1.5}]_OO_4$ should be:

$$TOF_T = \frac{j_{BET} \times A_{(111)}}{4 \times e \times N_T} = \frac{(0.1 \times 10^{-3}\ A \cdot cm^{-2}) \times (4.34 \times 10^{-19}\ m^2)}{4 \times (1.60 \times 10^{-19}\ C) \times 1.5} = 0.45\ s^{-1} \quad (6)$$

$NiFe(OH)_2$ in this work. To find out a rational density of the surface metal atoms (ρ), the value of 12.5 metal atoms nm^{-2} is adopted, which is based on the metal-metal distance of 2.83 Å for $NiFeO_xH_y$ measured in situ under OER conditions.[58,59] Thus, the TOF of $NiFe(OH)_2$ was calculated as

$$TOF = \frac{0.12\ mA \cdot cm^{-2}_{oxide}}{4 \times (1.60 \times 10^{-19}\ C) \times (12.5\ nm^{-2})} = 0.15\ s^{-1} \quad (7)$$

$Ni_aFe_{1-a}O_xH_y$. The TOF of $Ni_aFe_{1-a}O_xH_y$ were calculated based on reported works. The lower level is calculated using the data reported by Oscar Diaz-Morales et al.[39], where the TOF of the as synthesized NiFeOOH is calculated as

$$TOF = \frac{0.154\ mA \cdot cm^{-2}_{oxide}}{4 \times (1.60 \times 10^{-19}\ C) \times (12.5\ nm^{-2})} = 0.19\ s^{-1} \quad (8)$$

The upper level of $Ni_aFe_{1-a}O_xH_y$ is obtained by the work of Mikaela Görlin et al.[40], where a equals to 0.55. The TOF of $Ni_{0.55}Fe_{0.45}OOH$ was calculated as follows. To obtain the TOF value, we first calculated the BET normalized current density

$$j_{BET} = \frac{j_{Geo}}{(Metal\ Loading\ Mass\ per\ Geometric\ Area)\times\frac{Mr(Ni_{0.55}Fe_{0.45}OOH)}{Mr(Ni_{0.55}Fe_{0.45})}\times BET} \quad (9)$$

In this formula, the parameter $Mr(x)$ and BET represent the formula weight of x and the surface area per weight. The $Mr(x)$ is calculated as

$$j_{BET} = \frac{4.58\ mA{\cdot}cm_{Geo}^{-2}}{(10\ \mu g{\cdot}cm_{Geo}^{-2})\times\frac{90.42\ g{\cdot}mol^{-1}}{57.41\ g{\cdot}mol^{-1}}\times(27\ m^2{\cdot}g^{-1})} = 1.08\ mA\cdot cm_{oxide}^{-2} \quad (10)$$

Then the TOF was calculated as

$$TOF = \frac{j_{BET}}{4\times e\times\rho} = \frac{(1.08\ mA{\cdot}cm_{oxide}^{-2})}{4\times(1.60\times10^{-19}\ C)\times(12.5\ nm^{-2})} = 1.35\ s^{-1} \quad (11)$$

In all the above cases, the value of 12.5 metal atoms nm^{-2} (ρ) is used, which is based on the metal-metal distance of 2.83 Å for $NiFeO_xH_y$ measured in situ under OER conditions.[58,59]

IrO_2. The TOF of IrO_2 is calculated based on the work by Kelsey A. Stoerzinger et al.[37], where the TOF is calculated as

$$N_{(001)} = 1\times0 + \frac{1}{2}\times0 + \frac{1}{4}\times4 = 1\ atoms \quad (12)$$

$$A_{(001)} = a\times b = (4.545\ \text{Å})\times(4.545\ \text{Å}) = 2.07\times10^{-19}\ m^2 \quad (13)$$

$$TOF = \frac{j_{BET}\times A_{(001)}}{4\times e\times N_{(001)}} = \frac{(0.015\ mA{\cdot}cm_{oxide}^{-2})\times(2.07\times10^{-19}\ m^2)}{4\times(1.60\times10^{-19}\ C)\times1} = 0.048\ s^{-1} \quad (14)$$

RuO_2 and $Ba_{0.5}Sr_{0.5}Co_{0.8}Fe_{0.2}O_{3-\delta}$ (BSCF). The TOF value of RuO_2 and BSCF were directly taken from the work by W. T. Hong et al.[38], where the TOF value of RuO_2 and BSCF are 0.12 S^{-1} and 0.31 S^{-1}, respectively.

Inductively coupled plasma (ICP) analysis. The ICP analysis was conducted to determine the behavior of Al and Mn leaching in the solutions, which was performed on Agilent 720 Series ICP-OES with a detection limit of 0.02 ppm. The detailed ICP analysis results are listed in Supplementary Table 11, which indicates Al cations are partially leached out in the solution. To further investigate the metal-oxygen covalence in Al leached $[Mn]_T[Al_{0.5}Mn_{1.5}]_OO_4$, we have performed predictions for spinel $[Mn]_T[Al_{0.25}Mn_{1.5}]_OO_4$ and $[Mn]_T[Mn_{1.5}]_OO_4$. The results are shown in Supplementary Figure 11, which indicates spinel $[Mn]_T[Al_{0.5}Mn_{1.5}]_OO_4$ with Al vacancy are also excellent catalysts for OER.

OER free energy calculations. In alkaline solutions, OER occurs via the following elementary steps:

$$OH^- + * \rightarrow *OH + e^- \quad (15)$$

$$OH^- + *OH \rightarrow *O + H_2O + e^- \quad (16)$$

$$OH^- + *O \rightarrow *OOH + e^- \quad (17)$$

$$OH^- + *OOH \rightarrow * + O_2 + H_2O + e^- \quad (18)$$

where * denotes the adsorption sites on the catalyst surface. According to the above four steps, to obtain the pathway of OER, the free energies of *OH, *O and *OOH need to be identified. The computational hydrogen electrode (CHE) model[60] was used to calculate the free energies of the above-mentioned reaction intermediates, based on which the free energy of an adsorbed species is defined as

$$\Delta G_{ads} = \Delta E_{ads} + \Delta E_{ZPE} - T\Delta S_{ads} \quad (19)$$

where ΔE_{ads} is the electronic adsorption energy, ΔE_{ZPE} is the zero point energy difference between adsorbed and gaseous species, and $T\Delta S_{ads}$ is the corresponding entropy difference

between these two states. The electronic adsorption energy of the three intermediates is defined as

$$\Delta E_{ads} = E_{slab+OxHy} - E_{slab} - xE_O - yE_H \quad (20)$$

where $E_{slab+OxHy}$, E_{slab}, E_O, and E_H are the total electronic energy of the adsorption system, the clean slab, and the energies of O and H atom, respectively. The energy of O and H atom is referenced to (H_2O – H_2) and ½ H_2, respectively. Using this approach, the OER binding energy volcano and the free energy diagram have been successfully cited.[60,61] The corrections of zero point energy and entropy of the OER intermediates are summarized in Supplementary Table 10.

Data availability

The data supporting the findings of this study are available within the article and its Supplementary Information. Additional data are available from the corresponding authors upon reasonable request.

Code availability

The machine learning codes for making the covalency competition prediction are available at http://github.com/NTUyuanmiao/Covalency_Competition_Dominates_the_Water_Oxidation_Structure-Activity_Relationship_on_Spinel_Oxides.

References

1 Armstrong, R. C. et al. The frontiers of energy. *Nat. Energy* **1**, 15020 (2016).

2 Lewis, N. S. & Nocera, D. G. Powering the planet: Chemical challenges in solar energy utilization. *Proc. Natl. Acad. Sci.* **103**, 15729-15735 (2006).

3 Staffell, I. et al. The role of hydrogen and fuel cells in the global energy system. *Energy Environ. Sci.* **12**, 463-491 (2019).

4 Dau, H. et al. The mechanism of water oxidation: from electrolysis via homogeneous to biological catalysis. *ChemCatChem* **2**, 724-761 (2010).

5 Lee, Y., Suntivich, J., May, K. J., Perry, E. E. & Shao-Horn, Y. Synthesis and activities of rutile IrO_2 and RuO_2 nanoparticles for oxygen evolution in acid and alkaline solutions. *J. Phys. Chem. Lett.* **3**, 399-404 (2012).

6 Seitz, L. C. et al. A highly active and stable $IrO_x/SrIrO_3$ catalyst for the oxygen evolution reaction. *Science* **353**, 1011-1014 (2016).

7 Reier, T., Oezaslan, M. & Strasser, P. Electrocatalytic oxygen evolution reaction (OER) on Ru, Ir, and Pt catalysts: a comparative study of nanoparticles and bulk materials. *ACS Catal.* **2**, 1765-1772 (2012).

8 Yang, L. et al. Efficient oxygen evolution electrocatalysis in acid by a perovskite with face-sharing IrO_6 octahedral dimers. *Nat. Commun.* **9**, 5236 (2018).

9 Li, H. et al. Metal–oxygen hybridization determined activity in spinel-based oxygen evolution catalysts: a case study of $ZnFe_{2-x}Cr_xO_4$. *Chem. Mater.* **30**, 6839-6848 (2018).

10 Zhao, Q., Yan, Z., Chen, C. & Chen, J. Spinels: controlled preparation, oxygen reduction/evolution reaction application, and beyond. *Chem. Rev.* **117**, 10121-10211 (2017).

11 Chen, J. Y., Miller, J. T., Gerken, J. B. & Stahl, S. S. Inverse spinel $NiFeAlO_4$ as a highly active oxygen evolution electrocatalyst: promotion of activity by a redox-inert metal ion. *Energy Environ. Sci.* **7**, 1382-1386 (2014).

12 Zhou, Y. et al. Enlarged Co–O covalency in octahedral sites leading to highly efficient spinel oxides for oxygen evolution reaction. *Adv. Mater.* **30**, 1802912 (2018).

13 Duan, Y. et al. Mastering surface reconstruction of metastable spinel oxides for better water oxidation. *Adv. Mater.*, **31**, 1807898 (2019).

14 Grimaud, A. et al. Double perovskites as a family of highly active catalysts for oxygen evolution in alkaline solution. *Nat. Commun.* **4**, 2439 (2013).

15 Grimaud, A. et al. Activating lattice oxygen redox reactions in metal oxides to catalyse oxygen evolution. *Nat. Chem.* **9**, 457-465 (2017).

16 Yang, C. & Grimaud, A. Factors controlling the redox activity of oxygen in perovskites: from theory to application for catalytic reactions. *Catalysts* **7**, 149 (2017).

17 Goodenough, J. B. & Loeb, A. L. Theory of ionic ordering, crystal distortion, and magnetic exchange due to covalent forces in spinels. *Phys. Rev.* **98**, 391-408 (1955).

18 Wei, C. et al. Cations in octahedral sites: a descriptor for oxygen electrocatalysis on transition-metal spinels. *Adv. Mater.* **29**, 1606800 (2017).

19 Rong, X., Parolin, J. & Kolpak, A. M. A fundamental relationship between reaction mechanism and stability in metal oxide catalysts for oxygen evolution. *ACS Catal.* **6**, 1153-1158 (2016).

20 Zhou, Y. et al. Superexchange effects on oxygen reduction activity of edge-sharing $[Co_xMn_{1-x}O_6]$ octahedra in spinel oxide. *Adv. Mater.* **30**, 1705407 (2018).

21 Seh, Z. W. et al. Combining theory and experiment in electrocatalysis: Insights into materials design. *Science* **355**, 146 (2017).

22 Lee, Y.-L., Kleis, J., Rossmeisl, J., Shao-Horn, Y. & Morgan, D. Prediction of solid oxide fuel cell cathode activity with first-principles descriptors. *Energy Environ. Sci.* **4**, 3966-3970 (2011).

23 Suntivch, J., May, K. J., Gasteiger, H. A., Goodenough, J. B. & Shao-Horn, Y. A perovskite oxide optimized for oxygen evolution catalysis form molecylar orbital principles. *Science* **334**, 1383-1385 (2011).

24 Suntivch, J., Perry, E. E., Gasteiger, H. A. & Shao-Horn, Y. The influence of the cation on the oxygen reduction and evolution activities of oxide surfaces in alkaline electrolyte. *Electrocatal.* **4**, 49-55 (2013).

25 Yang, C., Fontaine, O., Tarascon, J. & Grimaud, A. Chemical recognition of active oxygen species on the surface of oxygen evolution reaction electrocatalysts. *Angew. Chem. Int. Ed.* **56**, 8652-8656 (2017).

26 Garcia, A. C., Touzalin, T., Nieuwland, C., Perini, N. & Koper, M. Enhancement of oxygen evolution activity of nickel oxyhydroxide by electrolyte alkali cations. *Angew. Chem. Int. Ed.* **58**, 12999-13003 (2019).

27 Ahneman, D. T., Estrada, J. G., Lin, S., Dreher, S. D. & Doyle, A. G. Predicting reaction performance in C–N cross-coupling using machine learning. *Science* **360**, 186-190 (2018).

28 Gawande, M. B. et al. Cu and Cu-based nanoparticles: synthesis and applications in catalysis. *Chem. Rev.* **116**, 3722-3811 (2016).

29 Sun, S. et al. Shifting oxygen charge towards octahedral metal: a way to promote water oxidation on cobalt spinel oxides. *Angew. Chem.* **131**, 6103-6108 (2019).

30 Dong, R. et al. Enhanced supercapacitor performance of Mn_3O_4 nanocrystals by doping transition-metal ions. *ACS Appl. Mater. Inter.* **5**, 9508-9516 (2013).

31 Liao, H. et al. A multisite strategy for enhancing the hydrogen evolution reaction on a nano-Pd surface in alkaline media. *Adv. Energy Mater.* **7**, 1701129 (2017).

32 Laffont, L. & Gibot, P. High resolution electron energy loss spectroscopy of manganese oxides: application to Mn_3O_4 nanoparticles. *Mater. Charact.* **61**, 1268-1273 (2010).

33 Wei, C. & Xu, Z. J. The comprehensive understanding of 10 mA cm^{-2}_{geo} as an evaluation parameter for electrochemical water splitting. *Small Methods* **2**, 1800168 (2018).

34 Sun, S., Li, H. & Xu, Z. J. Impact of surface area in evaluation of catalyst activity. *Joule* **2**, 1024-1027 (2018).

35 Jung, S., McCrory, C. C., Ferrer, I. M., Peters, J. C. & Jaramillo, T. F. Benchmarking nanoparticulate metal oxide electrocatalysts for the alkaline water oxidation reaction. *J. Mater. Chem. A* **4**, 3068-3076 (2016).

36 Wei, C. et al. Approaches for measuring the surface areas of metal oxide electrocatalysts for determining their intrinsic electrocatalytic activity. *Chem. Soc. Rev.* **48**, 2518-2534 (2019).

37 Stoerzinger, K. A., Qiao, L., Biegalski, M. D. & Shao-Horn, Y. Orientation-Dependent oxygen evolution activities of rutile IrO_2 and RuO_2. *J. Phys. Chem. Lett.* **5**, 1636-1641 (2014).

38 Hong, W. T. et al. Toward the rational design of non-precious transition metal oxides for oxygen electrocatalysis. *Energy Environ. Sci.* **8**, 1404-1427 (2015).

39 Diaz-Morales, O., Ledezma-Yanez, I., Koper, M. & Calle-Vallejo, F. Guidelines for the rational design of Ni-based double hydroxide electrocatalysts for the oxygen evolution reaction. *ACS Catal.* **5**, 5380-5387 (2015).

40 Görlin, M. et al. Tracking catalyst redox states and reaction dynamics in Ni–Fe oxyhydroxide oxygen evolution reaction electrocatalysts: The role of catalyst support and electrolyte pH. *J. Am. Chem. Soc.* **139**, 2070-2082 (2017).

41 Abild-Pedersen, F. et al. Scaling properties of adsorption energies for hydrogen-contaning molecules on transition-metal surfaces. *Phys. Rev. Lett.* **99**, 016105 (2007).

42 Kresse, G. & Furthmüller, J. Efficient iterative schemes for ab initio total-energy calculations using a plane-wave basis set. *Phys. Rev. B* **54**, 11169-11186 (1996).

43 Kresse, G. & Hafner, J. Ab initio molecular-dynamics simulation of the liquid-metal-armorphous-semiconductor transition in germanium. *Phys. Rev. B* **49**, 14251-14269 (1994).

44 Blöchl, P. E. Projector augmented-wave method. *Phys. Rev. B* **50**, 17953-17979 (1994).

45 Perdew, J. P., Burke, K. & Ernzerhof, M. Generalized gradient approximation made simple. *Phys. Rev. Lett.* **77**, 3865-3868 (1996).
46 Dudarev, S., Botton, G., Savrasov, S., Humphreys, C. & Sutton, A. Electron-energy-loss spectra and the structural stability of nickel oxide: an LSDA+U study. *Phys. Rev. B* **57**, 1505-1509 (1998).
47 Monkhorst, H. J. & Pack, J. D. Special points for Brillouin-zone integrations. *Phys. Rev. B* **13**, 5188-5192 (1976).
48 Blöchl, P. E., Jepsen, O. & Andersen, O. K. Improved tetrahedron method for Brillouin-zone integrations. *Phys. Rev. B* **49**, 16223-16233 (1994).
49 Svetnik, V. et al. Random forest: a classification and regression tool for compound classification and QSAR modeling. *J. Chem. Inf. Comp. Sci.* **43**, 1947-1958 (2003).
50 Jha, D. et al. Elemnet: Deep learning the chemistry of materials from only elemental composition. *Sci. Rep.* **8**, 17593 (2018).
51 Islam, M. et al. Study on the electrochemical reaction mechanism of $NiFe_2O_4$ as a high-performance anode for Li-ion batteries. *ACS Appl. Mater. Inter.* **9**, 14833-14843 (2017).
52 Du, Y. et al. XAFCA: a new XAFS beamline for catalysis research. *J. Synchrotron Rad.* **22**, 839-843 (2015).
53 Ravel, B. & Newville, M. ATHENA, ARTEMIS, HEPHAESTUS: data analysis for X-ray absorption spectroscopy using IFEFFIT. *J.Synchrotron Rad.* **12**, 537-541 (2005).
54 Yu, X., Diao, C., Venkatesan, T., Breese, M. & Rusydi, A. A soft x-ray-ultraviolet (SUV) beamline and diffractometer for resonant elastic scattering and ultraviolet-vacuum ultraviolet reflectance at the Singapore synchrotron light source. *Rev. Sci. Instrum.* **89**, 113113 (2018).
55 Wei, C. et al. Recommended practices and benchmark activity for hydrogen and oxygen electrocatalysis in water splitting and fuel cells. *Adv Mater.* **31**, 1806296 (2019).
56 Mishra, R. K. & Thomas, G. Surface energy of spinel. *J. Appl. Phys.* **48**, 4576-4580 (1977).
57 Farragher, A. Surface vacancies in close packed crystal structures. *Adv. Colloid Interface Sci.* **11**, 3-41 (1979).
58 Roy, C. et al. Impact of nanoparticle size and lattice oxygen on water oxidation on NiFeO x H y. *Nature Catal.* **1**, 820 (2018).
59 Friebel, D. et al. Identification of highly active Fe sites in (Ni, Fe) OOH for electrocatalytic water splitting. *J. Am. Che. Soc.* **137**, 1305-1313 (2015).
60 Nørskov, J. K. et al. Origin of the overpotential for oxygen reduction at a fuel-cell cathode. *J. Phys. Chem. B* **108**, 17886-17892 (2004).
61 Man, I. C. et al. Universality in oxygen evolution electrocatalysis on oxide surfaces. *ChemCatChem* **3**, 1159-1165 (2011).

Acknowledgements: This work was supported by Singapore Ministry of Education Tier 2 Grant (MOE-2018-T2-2-027) and the Singapore National Research Foundation under its Campus for Research Excellence And Technological Enterprise (CREATE) programme. Authors thank the Facility for Analysis, Characterization, Testing, and Simulation (FACTS) in Nanyang Technological University. This research used resources of the National Synchrotron Light Source II, a U.S. Department of Energy (DOE) Office of Science User Facility operated for the DOE Office of Science by Brookhaven National Laboratory under Contract No. DE-SC0012704. The authors also appreciate the XAS measurements from SSLS, SUV (Soft X-Ray-Ultraviolet) beamline. Y.S. and Z.X. thank Prof. Alexei Lapkin (University of Cambridge) for helpful discussion on ML concept and thank Prof. Lin Zeng (Southern University of Science and Technology) for helpful discussion on catalyst performance. H.Z. thanks the support from ITC via Hong Kong Branch of National Precious Metals Material (NPMM) Engineering Research Center, and the start-up grant (Project No. 9380100) and grants (Project No. 9610478 and 1886921) in City University of Hong Kong.

Author contributions: Z.X. and Y.S. proposed the research. Y.S., H.L. and Z.X. designed the experiments. Y.S. conducted DFT modelling and simulation. H.L. established the mathematical approach. H.L., J.W., S.S., B.C., and S.O. carried out the experiments. S.X., C.D., Y.D., J.W., J.W., Y.S., and H.L. conducted XAS characterizations. Y.S. wrote the manuscript. H.L., S.X., Y.D., M.B., S.L., H.Z., and Z.X. performed the analysis and revised the manuscript.

Competing interests: The authors declare no competing interests.